Minor Research Report

12-08-2022

0 Layman's summary

While our medical knowledge has considerably expanded over the last hundred years, there are still several complex problems that we have not yet been able to solve. These, among others, include stopping aging-related deterioration, the effective treatment of cancer and regeneration of damaged or defect body parts. However, biomaterials are becoming a more effective tool in combating these unfortunate conditions. They are defined as a substance, which has been designed to interact with living systems to steer the course of therapeutic or diagnostic procedures. Biomaterials come in many different shapes and sizes and, therefore, they can fulfil different purposes, such as improve function (*e.g.* contact lenses), provide stability (*e.g.* orthopedic implants), help the body recover (*e.g.* prosthetic grafts) or kill cancer cells during phototherapy (*e.g.*, gold nanoparticles). This report specifically focuses on biomaterials for tissue engineering (TE), which is a field that focuses on methods to replace, regenerate or improve different tissue types. Generally, this is done by three-dimensional (3D) printing of structures, or scaffolds, which optimally mimic the target tissue to facilitate its recovery.

The biomaterials used in TE often have passive properties similar to the native tissue. This can mean having appropriate mechanical strength and/or conductivity, providing a place for cell to attach, being degradable by the body (= biodegradability) and, most importantly, not being toxic to the body (=biocompatibility). However, while many materials that meet these requirements have been identified, there are still a lot of challenges regarding the external control over the regeneration process. This is because the body is a dynamic environment, which should be replicable by the biomaterial. Therefore, biomaterials with active properties, such as drug release over time, mechanical stimulus over time or control over their temperature, are currently in demand. In this regard, graphene-based materials (GBM) are becoming more and more popular as they both have incredible passive properties (light, strong, good thermal/electrical conductivity and biocompatible), as well as good potential for active properties. Firstly, GBM can convert near-infrared (NIR) light into heat, which allows for temperature control. Secondly, they can be functionalized with drugs, which can allow for controlled drug release, or with magnetic nanoparticles (NP), which in combination with an external magnetic field can lead to a mechanical stimulus. Despite high potential for TE, GBM are on their own not printable, which would be favorable to optimally mimic the complex structures of native tissues, so they should be combined with another printable biomaterial to make a stimuli-responsive, printable composite.

In this report, a magnetic- and thermo-responsive, printable biomaterial is reported, composed of magnetic, reduced graphene-oxide and a pectin hydrogel, which helps with printability. First, graphene oxide nanoparticles (GOn) were functionalized with iron nanoparticles, producing magnetic, reduced GOn (@rGOn) with an average particle size of 379.5 ± 161.2 nm, a saturation magnetization of 59.6 emu/g and maximum heating capacity under near-infrared (NIR) irradiation of 12.8 ± 0.2 °C. Then, the @rGOn particles were incorporated in a pectin (PEC) hydrogel (0, 2.5, 5 wt.%) and scaffolds were produced with an average fiber diameter of 1061 ± 25 μm, average pore size of 1306 ± 220 μm and a printing

quality of 68.8 ± 3.6 %. The printed @rGOn-PEC scaffolds showed a maximum saturation magnetization of 6.17 emu/g, considerably high conductivity (~1.1 · 105 S/m) and retained moderate ability of NIR light-heat conversion (ΔT = 7.9 ± 1.4 °C). This showed that the scaffolds still have magnetic properties and that they are able to produce sufficient heat. Lastly, biocompatibility of the material was assessed by indirect and direct methods, which points to no toxicity to cells but more research is necessary.

Overall, the final results of this project take a step towards having biomaterials for TE that can be externally stimulated to influence the regeneration process. Aside from TE, these scaffolds could also be used for cancer therapy as that requires an increase of at least 5.5 °C. Further research would look further into their biocompatibility and would assess their effect on the development of different tissues.

Magnetic- and thermo-responsive, printable graphene oxide-pectin composite material for tissue engineering applications.

Tom van de Kemp

In the field of tissue engineering (TE), materials responsive to external stimuli are highly useful because they can provide more control over the regeneration process. Recently, graphene-based materials (GBM) have been reported as highly suitable for providing an external stimulus when used as a filler material. This work presents a multi-responsive composite material of magnetized graphene oxide nanoparticles (GOn) and pectin hydrogel with a broad range of relevant TE properties. First, GOn were functionalized with iron nanoparticles, producing magnetic, reduced GOn (@rGOn) with an average particle size of 379.5 ± 161.2 nm, a saturation magnetization of 59.6 emu/g and maximum heating capacity under near-infrared (NIR) irradiation of 12.8 ± 0.2 °C. The @rGOn particles were incorporated in a tuneable pectin (PEC) hydrogel (0, 2.5, 5 wt.%) and scaffolds were produced with an average fiber diameter of 1061 ± 25 μm, average pore size of 1306 ± 220 μm and a printing quality of 68.8 ± 3.6 %. Printed @rGOn-PEC scaffolds demonstrated a maximum saturation magnetization of 6.17 emu/g, considerably high conductivity (~$1.1 \cdot 10^5$ S/m) and retained moderate ability of NIR light-heat conversion (ΔT = 7.9 ± 1.4 °C). Lastly, biocompatibility of the material was assessed by indirect and direct methods, but more research is necessary. Overall, these results provide the first steps towards a novel, multi-responsive biomaterial for application in tissue engineering.

---

1 Introduction

Tissue engineering (TE) emerged as a field to provide solutions to the challenges faced with traditional transplantation methods, such as organ shortage and rejection [1]. One of its general methodologies involves the three-dimensional (3D) printing of tissue-specific constructs, or scaffolds, which mimic the target tissue to facilitate successful recovery [2]. Many different types of materials are commonly used for the development of these scaffolds, such as ceramics (*e.g.* hydroxyapatite, bioactive glasses) [3, 4], synthetic polymers (*e.g.* poly-ε-caprolactone, poly-lactic acid) or natural polymers (*e.g.* alginate, gelatin) [4, 5] and composites thereof have already been explored. However, there are still major challenges related to the control over their biomechanical, biochemical and biological functionality.

Therefore, a state-of-the-art concept that is currently being explored is the fabrication of 'smart' scaffolds, which are able to supply and/or respond to stimuli beneficial to the

regeneration of the target tissue [6]. This can be done biochemically, for example through the controlled release of drugs, proteins or genes over time [7], or physically, for example by applying mechanical stress with shape-memory materials [8, 9] or with an external magnetic field [6, 10-12]. Lastly, a thermal stimulus can also be supplied, inducing hyperthermia either optically [13, 14] or magnetically [15, 16]. An effective methodology to establish stimuli-responsive properties in commonly used TE materials is the incorporation of nanofillers [6]. For example, nanoparticles (NP) responsive to photothermal irradiation (*e.g.* polydopamine (PDA) , gold-NP (Au-NP), graphene (G) [17-19])) might be used for thermal stimuli, whereas magnetic NP (*e.g.* iron oxides (Fe_2O_3, Fe_3O_4) [10]) can provide magneto-thermal or magneto-mechanical properties. Additionally, the addition of these nanofillers can improve mechanical strength of the base materials [20]. However, the biggest disadvantage of most NP (Au-NP, Fe_2O_3, Fe_3O_4) is their limited degradability, which can lead to bioaccumulation [21]. While graphene-based-materials (GBM) have been shown to be degradable by human neutrophil-derived myeloperoxidase (hMPO), or in neutrophil extracellular traps (NETs), and was reported as cleared from the system within 1 month *in vivo* in mice [22-24]. In this regard, GBM are emerging as promising candidates for use in the fabrication of 'smart' TE scaffolds owing to their relatively high biodegradability and inherent versatile properties.

By itself graphene already has an outstanding, wide range of properties for TE, including its incredibly low density (0.77 mg/m^2) [25], tensile strength (130 GPa) [26], Young's modulus (±1 TPa) [27], and remarkable thermal (±4000 W / mK) and electrical conductivity (10^4 - 10^5 S / m) [28, 29]. Moreover, the exfoliation of graphite (Gt) by ultrasonication allows for environmentally-friendly production of large batches of graphene, with minimal lateral dimensions. Ideally, an average lateral size of 100 nm is aimed for to minimize cytotoxicity risks in the body, while retaining surface chemistry and narrow size distribution [30, 31]. Graphene may also be modified for better interaction with the polymer matrix, to allow for easier modification or to improve biocompatibility. For example, oxidation yields graphene oxide (GO) and its new oxygen-containing functional groups improve polarity and allow for more surface functionalization. However, this disrupts the aromatic structure of graphene, reducing the electric and optical conductivity [13, 31, 32]. As a solution, the (thermal, chemical, or photo-) reduction of GO restores some of its original structure, while also retaining some of its polar groups [13, 33]. Therefore, altogether, GBM have already received a lot of interest for their use in TE scaffolds across a variety of tissue engineering applications [34, 35]. However, their combination with natural and/or synthetic biomaterials for the fabrication of stimuli-responsive materials exhibiting adequate biophysical, biochemical and biological function is still in the beginning.

For stimuli-responsive materials, GBM are primarily of interest due to their minimal band gap, to induce hyperthermia over a short period of time when exposed to near-infrared (NIR) irradiation. This is most commonly employed for cancer phototherapy applications [36], but could be combined with TE as well. In this line of thought, Bai *et al.* [37] already demonstrated *in vivo*, in mice, the high effectivity of dual functional GBM scaffolds for both cancer treatment and subsequent regeneration of the affected breast tissue. Additionally, mild hyperthermia (39.5 – 41.5 °C) was recently reported to promote osteogenesis [14, 15, 38].

Secondly, GBM have high affinity for further surface functionalization due to their large surface area [18]. This is of interest for 'smart' materials as it can further improve light-heat conversion ability by binding photo-thermally responsive NP [17-19]. Alternatively, magnetic NP can be attached to add magnetic properties [10]. The movement of magnetic NP under an external magnetic field results in small mechanical stresses to their environment, which was already shown to promote cell proliferation [39], and to guide stem cell differentiation [40]. Similar stimuli could be created when magnetized GBM are incorporated in scaffolds. However, while GBM are very versatile as fillers, the quality of the final scaffolds also rely largely on the base material. To optimally mimic the native tissue, it is highly desirable that the final composite is biocompatible and printable enough to replicate natural complex structures.

Natural polymers are very suitable as base material because of their resemblance to native extracellular matrix (ECM) components and ease of use in three-dimensional (3D) printing [41, 42]. Recently, pectin has attracted some attention as natural polymer for the fabrication of TE scaffolds. Mainly due to high tuneability of its biocompatibility, rheological behavior and mechanical properties [43-48]. Firstly, its cell-responsive properties are tuneable as a result of the absence of cell-adhesive and protease-cleavage sites in its original composition, which provides the opportunity to fine tune the cell response, for instance, via biofunctionalization with RGD-containing peptides [44]. Furthermore, its rheological behavior may be finely modulated by exploring pectin's inherent ionic gelation ability by controlling the concentration of available di- or trivalent ions (*e.g.* Ca^{2+}, Sr^{2+}, Al^{3+}) [45]. Lastly, the mechanical properties can be tuned through the incorporation of functional groups (*e.g.* methacrylate, norbornene groups) into the pectin backbone, which allows for chemical crosslinking to occur under UV-radiation, in the presence of a photo-initiator [44, 46, 47]. Regardless of these modifications, the mechanical strength remains relatively low compared to other non-hydrogel materials, but incorporation of GBM can help improve this significantly [49]. Therefore, pectin appears to be a versatile option to facilitate the production of 'smart' GBM scaffolds.

Altogether, the combination of magnetic GBM and pectin is expected to provide a lot of different parameters that may be optimized, resulting in a printable material with incredible flexibility. Ultimately, that would provide the ability to take more control over the biomechanical, biochemical and biological functionality of the fabricated scaffolds and thus the regeneration of the targeted tissue. Therefore, in this report, the design and fabrication of a new printable, thermo- and magnetic-responsive GBM/pectin hydrogel material is reported. First, magnetic GBM are synthesized and characterized. Then, the composite hydrogel is designed and evaluated for its printability. Finally, scaffolds of the GBM/pectin hydrogel are characterized for their relevant, stimuli-responsive properties and biocompatibility.

2 Materials & Methods

2.1 GBM production

GO was produced following the modified Hummers method [32]. Briefly, H_2SO_4 (160 ml) and H_3PO_4 (40 ml) were added to graphite (4 g) at room temperature (RT) under agitation. Then, the reactor was cooled to 11 °C and KMnO4 (24 g) was carefully added, followed by distilled water (600 ml), and H_2O_2 (26.5 ml) to reduce the excess $KMnO_4$. After resting overnight, the final solution was washed with distilled water by centrifuging (2000 rpm, 5 min), decanting and resuspending until a neutral pH was reached. Finally, the resulting solution was ultrasonicated for 8 hours to produce GO nanoparticles (GOn).

Subsequently, the GOn was resuspended at 1 mg/ml and exposed to UV irradiation for 8 hours in order to produce reduced GOn (rGOn). Ultimately, the rGOn was magnetized using a previously established protocol [50]. Briefly, $FeCl_2 \cdot 4H_2O$ (1 g / 100 ml) was added to GOn solution and the resulting solution ultrasonicated for 10 minutes. Then, by adding NH_3 solution the pH was adjusted to 9, after which the temperature was increased to 180 °C. The solutions were left to react for 10 hours, under agitation, and rested overnight. Lastly, the magnetized GOn (@GOn) was washed with distilled water employing permanent neodymium magnets (Supermagnete, Germany) until a clear supernatant was achieved. It is of note, that the high temperatures of the magnetization process have been shown to thermally reduce the GOn [51]. Therefore, after magnetization, @GOn will be referred to as magnetic reduced GOn (@rGOn). The washed @rGOn was resuspended at 90 mg/ml and stored at 4 °C.

2.2 GBM characterization

Dispersions of produced GOn, rGOn, and @rGOn, at a concentration of 50 μg mL^{-1}, were imaged using transmission electron microscopy (TEM, JEOL, JEM 1400 TEM, Tokyo Japan) to analyze particle morphology and perform size measurement. Per sample, 10 μL was dropped on a carbon coated TEM grid and allowed to dry for 1 min, after which excess material was removed with filter paper.

Moreover, @rGOn particle size distribution was measured using dynamic light scattering (DLS, LS230 particle size analyzer, USA) on particles dispersed in water at a concentration of 100 μg mL^{-1}. Additionally, the infrared spectra of GOn, rGOn, and @rGOn were obtained out of dehydrated samples employing a VERTEX 70 FTIR spectrometer (Bruker, Karlsruhe, Germany) in transmittance mode at RT. Spectra were recorded by averaging 64 scans over the wavenumber range between 4000 and 400 cm^{-1}.

2.3 Pectin synthesis

First, low methoxyl (LM) citrus pectin (Classic CU701, 86% galacturonic acid content, 37% degree of methylation, Herbstreith & Fox, Germany) was purified as previously described

[52], which is the main form of pectin used in this report (referred to as PEC). Briefly, after completely dissolving LM citrus pectin in ultrapure water (1 wt.%, Milli-Q, MilliPore), the pH was adjusted to 6 and the solution was filtered with 0.80 μm, 0.45 μm and 0.22 μm filters (MCE, Millipore), activated charcoal (2 wt.%, Norit SX Plus, Norit) was added and stirred for 1 hour at RT. Subsequently, twice, the suspension was centrifuged (27000g, 1 hour), carefully decanted and stirred again for 30 minutes. Finally, the remaining supernatant wasfrozen, lyophilized and stored at -20 °C.

In order to allow cell adhesion, PEC was modified with an integrin-binding peptide CGGGGRGDSP (Genscript, cell-adhesive domain underlined) using carbodiimide chemistry, according to an adaptation of existing protocols [53]. In short, PEC was dissolved (1 wt.%) in ultrapure water and 4-(4,6-Dimethoxy-1,3,5-triazin-2-yl)-4-methylmorpholinium chloride (DMTMM) was added (0.67 g DMTMM / g PEC) and stirred for 30 minutes, to achieve 50% activation of PEC carboxylic groups. Then, the peptide was added (75 mg / g PEC) and left to react for 24 hours. After the reaction, RGD-modified PEC (RGD-PEC) was dialyzed, lyophilized and stored at -20 °C. The coupling efficiency was evaluated through colorimetric DC Protein assay (Bio-Rad) according to modified manufacturer's instructions [44].

Additionally, for initial proof-of-concept experiments, PEC was functionalized with different functional groups (pectin-methacrylate (PECMA), pectin-norbornene (PECNOR)) according to established protocols [44, 47]. Briefly, to synthesize PECMA, PEC was dissolved (1.25 wt.%) in phosphate buffered saline (PBS) at RT and methacrylic anhydride (Sigma-Aldrich) was added dropwise under agitation, while the pH was kept at 8 through addition of NaOH (2.5 mM). After 24 hours of reaction, PECMA was collected by precipitating twice in a ten-fold excess of cold (4 °C) acetone, then re-dissolved in ultrapure water and purified by dialysis. Lastly, the solution was sterilely filtered using 0.22 μm filters, lyophilized and stored at -20 °C for further use.

For the synthesis of PECNOR, PEC was dissolved in ultrapure water (1 wt.%) under agitation and the Dowex 50W ion exchange resin (Acros Organics) was added and left for 3 hours, after which the solution was centrifuged, the supernatant filtered with 0.22 μm filter and the pH adjusted to 6.5 with tetrabutylammonium (TBA, Sigma-Aldrich) to produce tetrabutylammonium salt (PEC-TBA), which could be lyophilized and stored at -20 °C. PEC-TBA was dissolved (1wt.%) in dimethyl sulfoxide (DMSO) and allowed to react for 1 hour, under agitation, with carbic anhydride (CA, Acros Organics) at a 1-fold molar excess to hydroxyl groups in the polymer backbone. Then, the PECNOR solution was dialyzed, treated with activated charcoal (1 g / g of polymer) as described above. Ultimately, the pH of the solution was neutralized (pH = 7), frozen, lyophilized and stored at -20 °C for later use.

2.4 Formation of (@rGOn-)pectin hydrogels

In order to fabricate hydrogels, PEC was dissolved at (2.5 wt.%) in ultrapure water, to which NaCl (0.9wt.% final concentration) and @rGOn (0, 2.5, 5 wt.%) was added. After complete polymer dissolution, $CaCl_2$ was added (9 mM) and left for 45 minutes to induce sufficient

gelation in the hydrogels for printing. For cell culture experiments, both PEC and RGD-PEC were mixed to achieve a final concentration of 500 μM of RGD in the final hydrogel.

Furthermore, to PECMA and PECNOR hydrogels, lithium phenyl-2,4,6-trimethylbenzoylphosphinate (LAP) was added at different concentrations (2-20 mM) as photo-initiator and dithiothreitol (DTT, 2-8 mM) as crosslinker. Afterwards, the hydrogels were exposed to UV-light (365 nm, Hamamatsu) at 7 mW/cm^2 up to 5 minutes to induce photopolymerization.

Additionally, rheological properties were evaluated with a Kinexus Pro rheometer (Malvern), to determine the gelation time. Specifically, hydrogels were compressed to 20% of their initial height before frequency sweeps from 0 to 1000 Hz were performed at RT over a period of 100 minutes. Briefly, $CaCl_2$ was added to ungelated polymer solution, mixed well and immediately transferred to parallel plates (0.5 mm distance) to start the measurement.

2.5 Extrusion-based 3D printing

Scaffolds were printed according to previously described protocols [44]. The pre-crosslinked hydrogel was loaded into a syringe equipped with differently sized, cylindrical nozzles (0.41 mm, 0.33 mm, 0.25 mm, Nordson EFD) using a commercial Regemat 3D V1 printer (Regemat 3D, Spain). The manufacturer's software was used to control the printer and generate the G-code for the final scaffold structure. Square (12.5x12.5 mm) scaffolds with fixed inter fiber spacing (IFS, 1.5 mm, 2 mm, 2.5 mm) and height (2, 4, 6 layers) were fabricated using a flow speed of 2 mm/s, travel speed of 4.6 mm/s and maximal retraction speed (99.9 mm/s).

After printing, scaffolds were transferred to a bath of $CaCl_2$ (200 mM, 10 minutes) for further gelation to fix their printed shape. Scaffolds were cut into circular meshes using an 8 mm biopsy punch to fit in a 48-well cell culture plate.

The fiber diameter and printing accuracy were evaluated from images captured with a standard stereomicroscope (Olympus SZX10, magnification 1.63x). Printing accuracy was computed through the quality number (Q) defined as the ratio between measured and expected visible area of the pores:

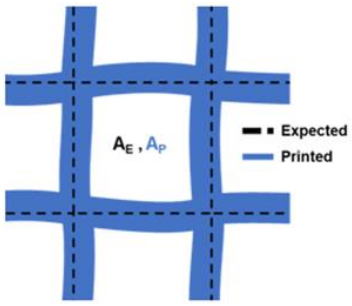

$$Q = \frac{A_{measured}}{A_{expected}} * 100\% \quad ,$$

$$A_{expected} = n_{pores} \times \left(IFS - \emptyset_{fiber\ diameter}\right)^2$$

While the $A_{measured}$ was determined with ImageJ (National Instruments, USA), applying the binary and measurement function.

2.6 Characterization of (@rGOn-)pectin samples

The influence of @rGOn content on the mechanical strength of the hydrogel was evaluated by dynamic mechanical analysis (DMA) using a dynamic mechanical analyzer (DMA 242E Artemis, Netzch). Stress-relaxation tests were performed at 37 °C in compression mode, applying a 20% strain and allowing the samples to recover for 15 minutes total. Relaxation time was determined by normalizing the curves to the maximum produced force of the sample, fitting a logarithmic curve and determining the time to relax to half of the initial force. Ultimately, an exponential decay model was also used to fit the curves, out of which the relaxation times were determined using the same procedure. Additionally, a rough estimate of the elastic modulus was approximated by dividing the maximum produced force by the applied strain (supplementary figure 2).

The magnetic responsive behavior of dried rGOn, @rGOn and its corresponding scaffolds at (0, 2.5 and 5 wt.%) were evaluated by superconducting quantum interference device (SQUID, Quantum Design, Germany) at 310 K applying a magnetic field up to ±50.000 Oe.

Conductivity of dried samples was determined utilizing a 4-point-probe method (2400 series, Keithley Instruments). Prior to measurement, @rGOn-pectin hydrogel squares at different @rGOn concentrations (0, 2.5, 5 wt.%) were dried in a vacuum oven at 40 °C overnight. The dried sample thickness and resistance was measured at RT, after which their sheet resistance was calculated, using:

$$R_{sheet} = -\pi * \frac{R_{measured}}{\ln(2)}$$

Then, conductance was computed as the inverse of the sheet resistance multiplied by the thickness, averaging three measured replicates per group.

The ability of our samples to convert light-to-heat was evaluated using a previously established method [13]. Briefly, samples (rGOn, @rGOn, PEC, @rGOn(2.5 wt.%)-PEC, @rGOn(5 wt.%)-PEC) were placed in a 48-well plate inside a benchtop incubator at 37 °C and irradiated with a LED-based source with peak emission around 810 nm (NIR region) and irradiance of 150 mW/cm^2, for a period of 30 minutes. The temperature was measured every 30 seconds using a thermocouple data logger (Pico TC-08 USB) employing the PicoLog data-logging software. Three replicates were used per condition with water as control and presented as their temperature difference (ΔT) over time, normalized to the temperature increase of water.

2.7 In vitro cell culture

Biological studies were performed using human neonatal dermal fibroblasts (hNDFs). Cells were cultured in Dulbecco's modified Eagle's medium (DMEM, ATCC) supplemented with fetal bovine serum (FBS, Gibco) 10% and penicillin/streptomycin (Sigma) 1% at 37 °C in a humidified atmosphere, containing 5% CO_2. Before cell culture experiments, samples were

disinfected using ethanol (EtOH) at 95% for 30 minutes, 80% for 15 minutes, 70% for 15 minutes and then washed 3 times with Hanks' balanced salt solution (HBSS) before incubating in complete cell culture media overnight.

2.8 Cytotoxicity assays

Cytotoxicity of (@rGOn-)PEC hydrogels was first evaluated by indirect contact test according to ISO10993-5, with the toxicity limit defined at 70%. Briefly, both disinfected and undisinfected hydrogels (100 μL) with different @rGOn contents (0, 2.5, 5 wt.%) were incubated in culture media for 24 hours, before exposing the hNDFs (passage number = 7) to the extracts for another 24 hours and measuring metabolic activity, setting unexposed cells as 100% viability.

Similarly, disinfected scaffolds of different @rGOn contents (0, 2.5, 5 wt.%) were incubated in culture media for 24 hours, before cell seeding. hNDFs were seeded (passage number = 15) onto the scaffolds at a concentration of $5x10^5$ cells per sample, completely covering the mesh, and were allowed to adhere overnight before refreshing culture media. At both day 1 and 7, metabolic activity was measured and fixation done for confocal imaging.

Metabolic activity of the cells was evaluated by resazurin assay, as previously described [44]. In short, resazurin was diluted in complete culture media (20 %v/v, resazurin sodium salt (0.1 mg/ml), Sigma-Aldrich) added to cells and incubated for 2 hours. Samples were measured using a microplate reader (Synergy MX, Biotek) at 530/590 nm excitation/emission filters, with at least two samples per group.

Immunofluorescence staining was performed on samples to show cell attachment and morphology. Samples were fixed and stained with DAPI (Vector Labs) and phalloidin (1:40, Molecular Probes-Invitrogen) solutions according to previously a described protocol [44]. Briefly, samples were washed 3 times with HBSS before, fixing with 4 %v/v paraformaldehyde for 30 minutes and washing again 3 times with HBSS. Then, samples were incubated in blocking solution (1 w/v% bovine serum albumin in HBSS) for 1 hour at RT and left overnight. Subsequently, samples were incubated with primary and secondary antibodies and washed. Samples were visualized by confocal microscopy (CLSM, Leica SP5AOBS, Leica Microsystems).

2.8 Statistical analysis

One-way or two-way ANOVA with post-hoc Tukey's test were performed to compare group means depending on the available group sizes. Data was displayed as mean ± standard deviation (SD). Differences were considered significant at a p-value below 0.5. If group size allowed, at least three samples were compared for each group. All results were processed with GraphPad prism V9.

3 Results

3.1 Production of @rGOn

Before the particles could be used, they had to be magnetized and characterized. First, @rGOn was produced from rGOn using an adaptation of previously established methods [32]. As the magnetization was successful, the particles could be washed and separated from remaining contaminants using their magnetic properties.

The particle size was determined using DLS on GBM water dispersions (100 μg mL^{-1}), (Figure 1C). rGOn particles presented a size of 298.6 ± 110.4 nm, slightly smaller than @rGOn particles (379.5 ± 161.2 nm). Furthermore, TEM images (Figure 1B) revealed particle sizes in the same order of magnitude, as well as well distributed iron nanoparticles (~ 40 nm) at the surface of the rGOn sheets.

After the magnetization process, a change in color (brownish to black), as well as lower aqueous stability was observed for @rGOn particles (Figure 1E). Analysis by DLS established that the zeta (ζ)-potential of @rGOn (-24 ± 4.45 mV) was lower than that of rGOn (-48.1 ± 5.61 mV). Moreover, there was an absence of peaks corresponding to hydroxyl groups (-OH, 3390 cm^{-1}) in the FTIR spectra of @rGOn (Figure 1D) [54].

The magnetization curves of the particles were plotted (Figure 1F), out of which a saturation magnetization of 59.6 emu/g was determined for @rGOn, the rGOn particles were confirmed to be non-magnetic. The ability of the particles to convert NIR light into heat was also determined (Figure 1G), with @rGOn presenting higher capacity of heat production (rGOn, ΔT_{final} = 7.3 ± 0.4 °C; @rGOn, ΔT_{final} = 12.8 ± 0.2 °C).

3.2 Formation of (@rGOn-)pectin hydrogels

To ensure that the composite material was suitable for printing, both the viscosity before printing had to be modulated, as well as the shape retention after printing. The addition of @rGOn did not noticeably affect the viscosity of the polymer solution. However, as the polymer solution was still too liquid for printing purposes, the viscosity of the hydrogel still had to be modulated to achieve a printable filament. Different concentrations of $CaCl_2$ (0, 3, 6, 9, 12 mM) were added to modulate the viscosity (Figure 2A). The addition of 9 mM achieved the desired result. Analysis of the rheological behavior showed that gelation occurred within 35 seconds but that the storage modulus kept increasing for a longer period of time (Figure 2B). After the printing process, different methods to fix the final hydrogel structure were explored. Photo-crosslinking using the functional groups of PECMA and PECNOR was unsuccessful, regardless of photo-initiator (LAP) and crosslinker (DTT) concentration or UV-exposure time. As a result, only external gelation in a bath of $CaCl_2$ could be used post-printing to achieve shape-retention. A $CaCl_2$ bath of at least 45 mM for 10 minutes resulted in adequate shape retention but 200 mM was used to ensure sturdy hydrogels.

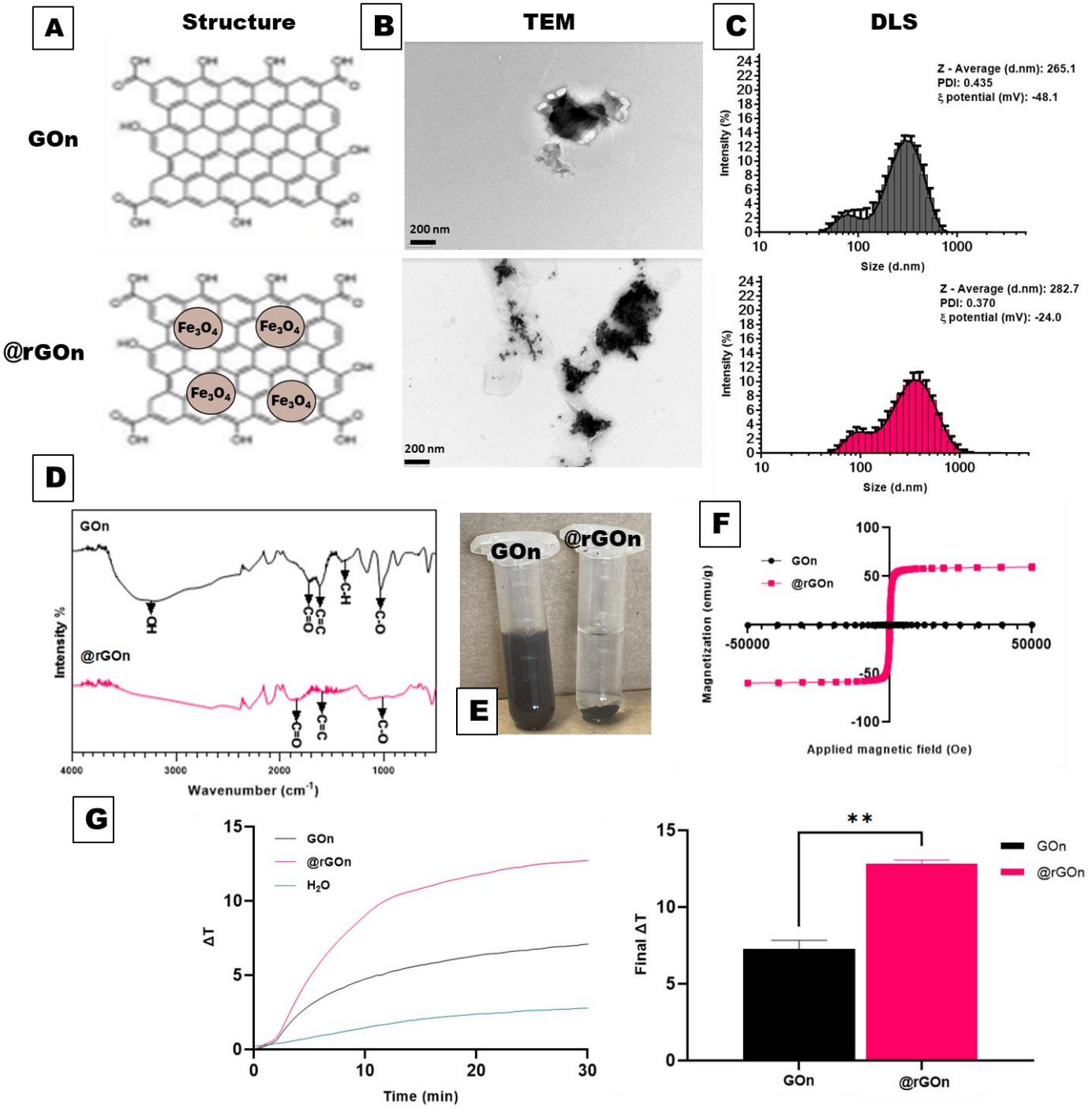

Figure 1: Characterization of graphene oxide nanoparticles (GOn) and magnetized GOn (@rGOn). A) Molecular structures of GOn and @rGOn. B) Transmission Electron Microscopy (TEM) shows surface morphology and distribution of iron nanoparticles at @rGOn surface. C) Particle size distributions as quantified by dynamic light scattering (DLS). D) Fourier Transform Infrared (FTIR) spectra shows absence of -OH peak in @rGOn. E) Digital images of GOn and @rGOn, revealing that the latter tends to precipitate in water, as expected in the simultaneous magnetization and reduction method employed. F) Magnetization curves quantified by superconducting quantum interference device (SQUID). G) Temperature variation (Δ*T*) over time (*left*) and final ΔT (*right*) after near-infrared (NIR) irradiation (n=3).

3.3 Printing of (@rGOn-)pectin hydrogels

Printing parameters and scaffold dimensions were optimized to successfully fabricate suitable scaffolds (Figure 2C). First, different nozzle sizes (0.41, 0.33, 0.25 mm) were

evaluated for the fiber diameter they produced. While the difference with the fiber diameter of the 0.33 mm nozzle (1181 ± 34 µm) was only slight, the 0.25 mm nozzle produced the thinnest fibers (1061 ± 25 µm). Smaller nozzle sizes resulted in needle clogging .

There was no clear, distinct statistic difference between the groups comparing printing accuracy and layer height/pore size, but a trend could be observed. Overall, printing accuracy decreased with increasing layer height and decreasing pore size. The maximum number of layers with minimal pore size was determined, where the accuracy did not decrease below 65%. The final scaffolds used for further characterization were printed with 2.5 mm pore size at 5-layer height, resulting in an overall printing accuracy of 68.8 ± 3.6 %.

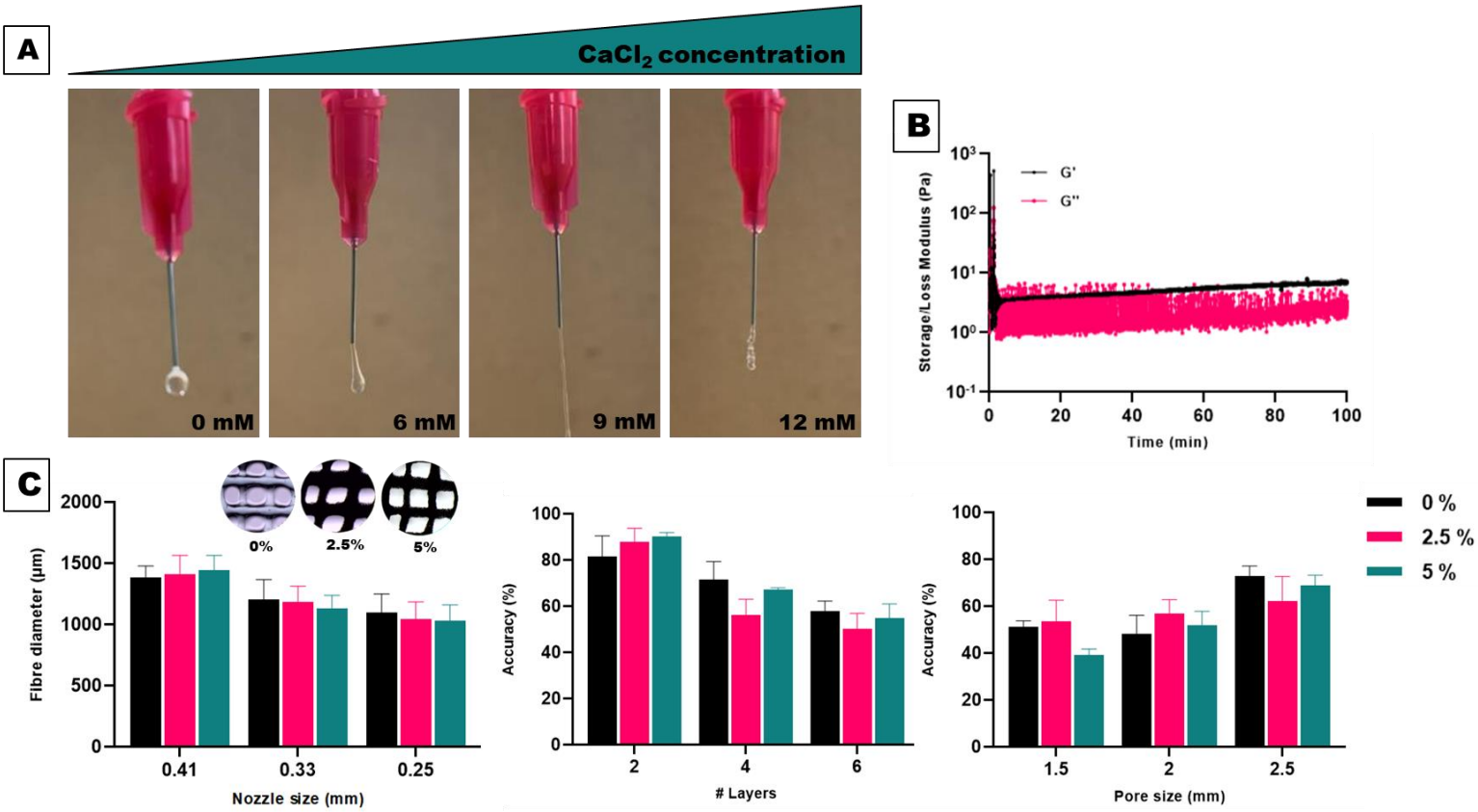

Figure 2: Evaluation of the printability of the @rGOn-PEC composite hydrogel. A) Modulation of the viscosity through addition of different $CaCl_2$ concentration (0, 6, 9, 12 mM). B) Frequency sweep to determine gelation time upon addition of $CaCl_2$ (9 mM). C) Evaluation of printing parameters, left-to-right; nozzle size vs fiber diameter, layer height vs printing accuracy, pore size vs printing accuracy.

3.4 Properties of (@rGOn-)pectin hydrogels

The GBM materials were then characterized for relevant TE properties, including mechanical, thermal, electrical and magnetic. Firstly, the ability of @rGOn to improve the hydrogels mechanical integrity was characterized through stress-relaxation tests and was defined by their relaxation times (Figure 3A). After application of a 20% strain, the samples

loaded with @rGOn (2.5 wt.%, 108 s; 5 wt.%, 60s) recovered faster than just PEC hydrogels (0 wt.%, 168 s).

Secondly, to ensure the @rGOn-PEC hydrogels are responsive to a magnetic field, their magnetization was evaluated (Figure 3-D,E). This confirmed that pectin hydrogel (0 wt.%, 0 emu/g) by itself is not magnetic and, similarly, that increasing the loading of the @rGOn, increased the magnetization of the scaffolds (2.5 wt.%, 2.98 emu/g; 5 wt.%, 6.17 emu/g). Interestingly, compared to the pristine @rGOn powders, the @rGOn-PEC scaffold with the highest loading (5 wt.%), had a ~10 times lower saturation magnetization (59.6 emu/g vs 6.17 emu/g, respectively).

Moreover, as graphene is known for its good electrical properties, which can be useful for TE, the conductivity of the dried materials was measured (Figure 3-F). The lower loading (2.5 wt.%) of @rGOn was unable to affect the conductivity of the dried hydrogel compared to the PEC (0 wt.%) control, yet doubling the @rGOn concentration (5 wt.%) did almost double the conductivity.

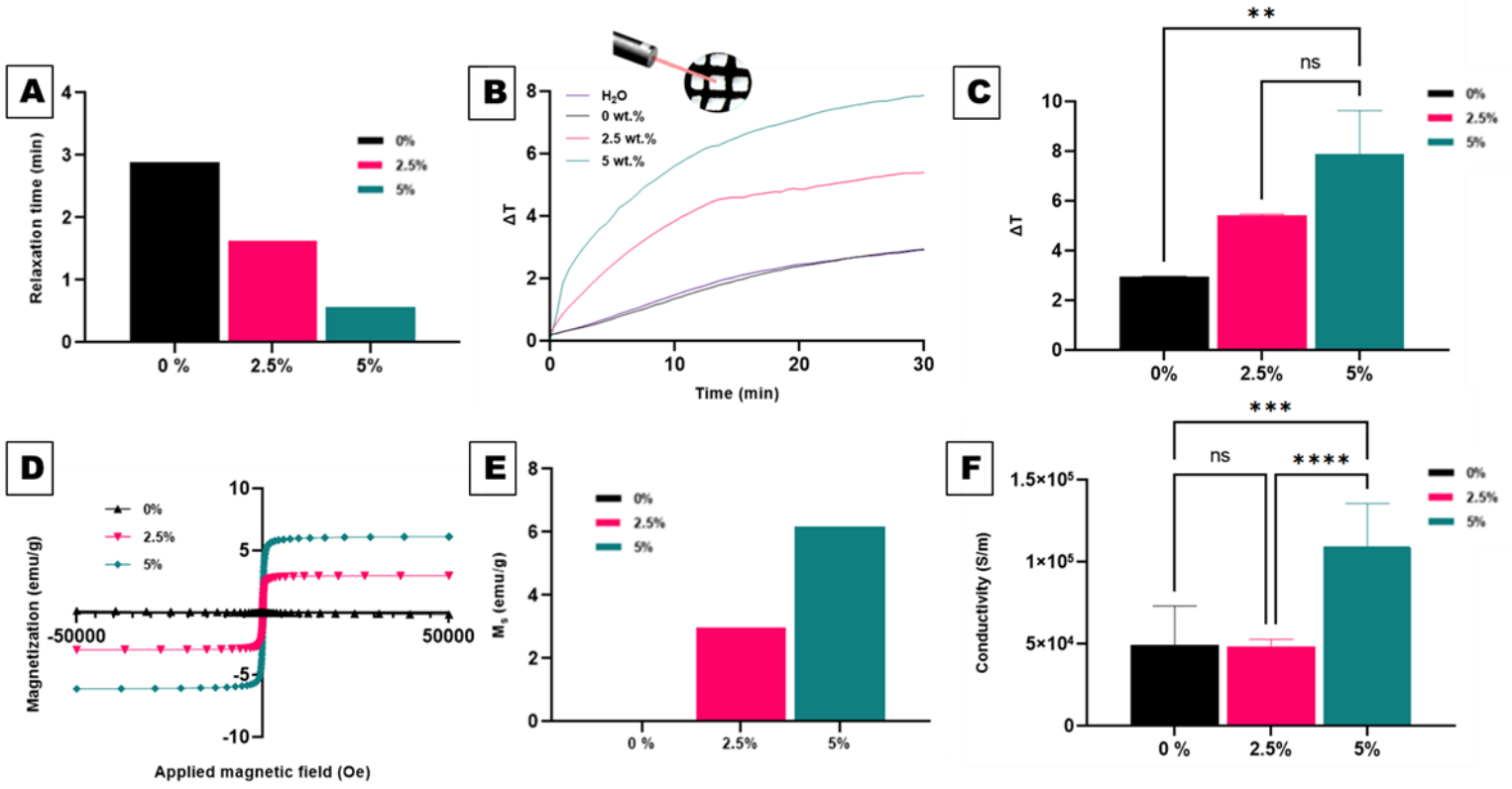

Figure 3: Characterization of @rGOn (0, 2.5, 5 wt.%) -Pectin composite hydrogel properties. A) Relaxation times quantified through dynamic mechanical analysis (DMA, stress-relaxation test). B) Change in temperature (ΔT) over time under near-infrared (NIR) irradiation. C) Final ΔT after NIR irradiation (n=3). D) Magnetization curves quantified by superconducting quantum interference device (SQUID). E) Saturation magnetization increases with @rGOn content. F) Conductivity at different @rGOn loading (0, 2.5, 5 wt.%).

Lastly, to confirm the scaffolds are responsive to NIR light, the temperature increase (ΔT) of the samples under NIR irradiation was evaluated (Figure 2-B,C). Again, with increasing @rGOn concentration, an overall increase in ΔT was observed inside the scaffolds. The pectin only scaffold (0 wt.%) showed a slight temperature increase (ΔT_{final} = 1.38 ± 0.1 °C) but this was similar to the control (H_2O) and a result of the ambient temperature increase due to the warming of the NIR system. Notably, all concentrations were able to sufficiently increase the temperature under NIR irradiation (2.5 wt.%, ΔT_{final} = 5.4 ± 0.04 °C ; 5%, ΔT_{final} = 7.9 ± 1.4 °C).

3.5 Cell response to (@rGOn-)pectin hydrogels

The cytotoxicity of the @rGOn-PEC hydrogels was first assessed through the indirect contact assay, to assess if any particles would leach out of the samples (Figure 4-A). Additionally, to find out if a disinfection procedure would affect the cell viability, the same experiment was performed on disinfected samples. Upon indirect contact, no drops in cell viability were found between groups (0 wt.%, 2.5 wt.%, 5 wt.%).

Then, cells were seeded on top of @rGOn-PEC hydrogels to assess cell attachment and biocompatibility over a longer period of time. During the incubation before cell seeding, scaffolds swelled up considerably and became very fragile, resulting in the loss of several samples due to breakage when transferring them onto well plates. The most intact samples were used for imaging, whereas metabolic assays were performed more on imperfect samples. DAPI/Phalloidin stain visualized some cell attachment (Figure 4-C) after 7 days in the 0 and 2.5 wt.% groups, the 5 wt.% group could not be stained successfully. Resazurin assay showed a large drop in metabolic activity at the seventh day across all except the 5 wt.% groups (Figure 4-B).

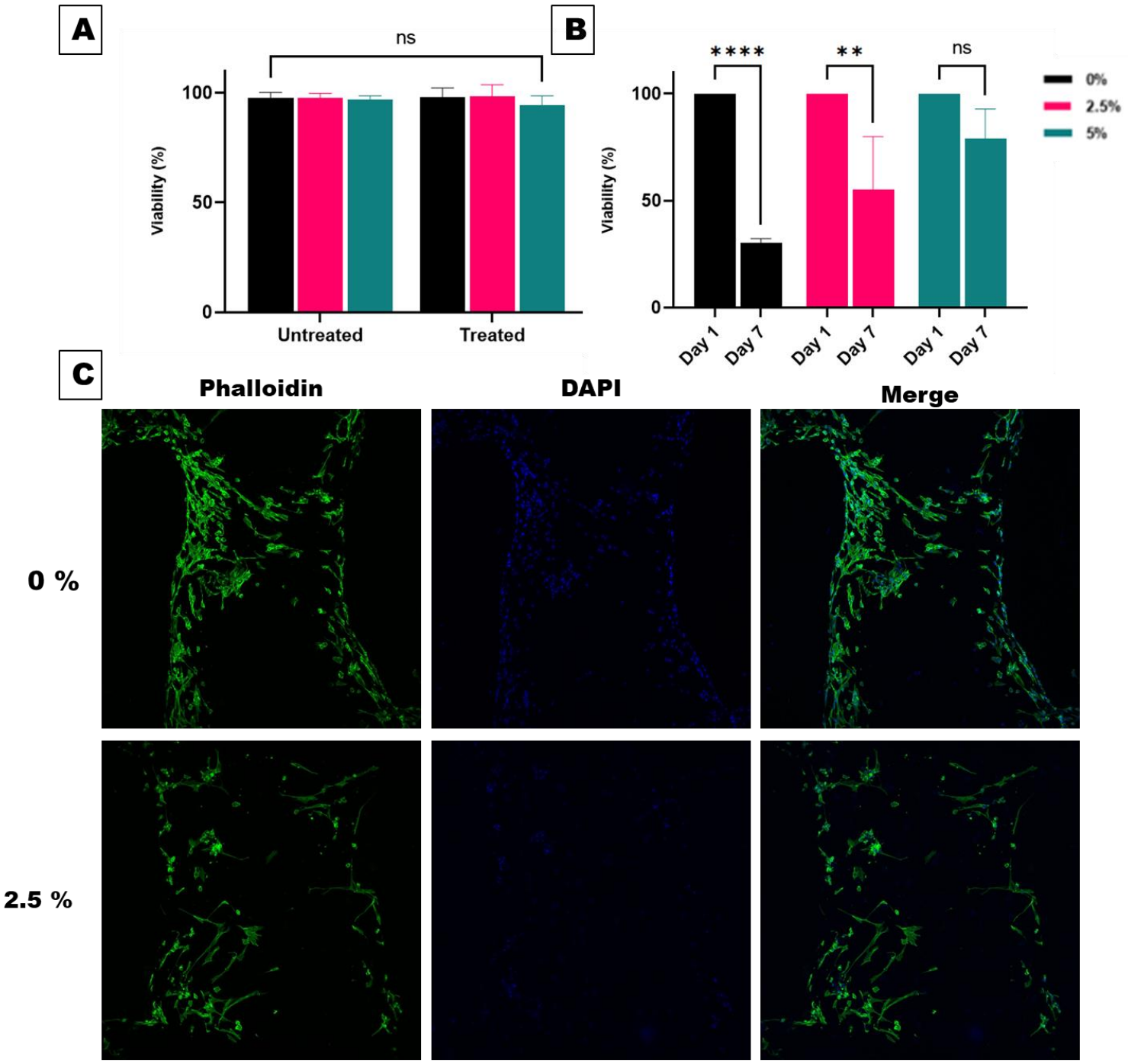

Figure 4: Biocompatibility of @rGOn(0, 2.5, 5 wt.%)-PEC hydrogels. A) Cell viability after 24 hours of indirect contact (*ISO10993-5*) as evaluated by resazurin assay. B) Cell viability after 1 and 7 days upon seeding on @rGOn(0, 2.5, 5 wt.%)-PEC scaffolds as evaluated by resazurin assay. C) Confocal images (10x magnification) of DAPI/Phalloidin stain of @rGOn(0, 2.5 wt.%)-PEC scaffold fragments after 7 days *(staining of 5 wt.% samples was unsuccessful)*.

4 Discussion

Firstly, magnetic nanoparticles were successfully produced from GOn through a previously established magnetization process [50]. The particles could now be straightforwardly washed with a novel method, by magnetically separating the @rGOn from non-magnetic waste products. An increase in particle size (298.6 ± 110.4 nm vs 379.5 ± 161.2 nm) was observed after magnetization by DLS measurement. The addition of iron particles on the GOn surface, as well as the aggregation observed in TEM are suggested as the main contributors to this size increase. This is likely the result of the high temperature (180 °C) used during the magnetization process, which has been reported to thermally reduce GO materials [55]. Reduction of GO makes them more hydrophobic resulting in more hydrophobic interactions in water and therefore more aggregation. This lower aqueous stability is also quantitatively supported by the lower zeta (ζ)-potential that was measured for @rGOn (-48.1 ± 5.61 mV vs -24 ± 4.45 mV), as particles with a zeta (ζ)-potential higher than ±30 mV are generally considered stable [56]. Moreover, this further reduction was also demonstrated by the FTIR spectra, as the relevant peaks corresponding to hydroxyl groups (-OH, 3390 cm^{-1}) were absent in @rGOn [54]. Lastly, reduction of GO has been reported to reduce its bandgap, which improves its absorption and thus explains the observation of an improved ability to convert NIR light into heat [57].

After synthesis of different types of pectin, @rGOn was incorporated at 0, 2.5 and 5 wt.% in the unmodified formulation, PEC, to create a printable composite material. It was impossible to induce any strong shape-retention in the composites of @rGOn with neither PECMA, nor PECNOR, through photo-crosslinking methods. The outside of the gels strengthened noticeably, yet the inside always remained runny and malleable, regardless of optimization. Most likely, this was caused by @rGOn's high absorption in the 300 nm range [58], which was used to crosslink the polymers, preventing any effective penetration of the UV-radiation into the hydrogel. However, it may be noted that this was already observed when GOn was incorporated into the hydrogel. Therefore, the higher absorption of @rGOn as a result of the reduction that took place during the magnetization, did not make the difference for photo-crosslinking ability. Thus, functionalization of the PEC was deemed unnecessary and external gelation with $CaCl_2$ was opted for as effective, alternative method for maintaining printed form of the PEC hydrogels.

Similarly, external gelation was used to modulate the @rGOn-PEC solution to a printable viscosity. However, the printability of the hydrogel is severely limited. Firstly, this is evident when comparing nozzle size to actual diameter of produced fibers, as the actual fiber diameter is roughly ~ 3 times higher than the nozzle size. This is a result of inherent shear thinning behavior of hydrogels, where after extrusion the shear recovery results in the fibers thickening. During printing, this same process limits the accurate deposition of consecutive layers, because it prevents pausing the extrusion while repositioning for the next layer. Simultaneous retraction of the piston is supposed to relieve pressure to stop this from happening, but even at maximal retraction speed (99 mm/s) the issue was not resolved.

Then, a variety of relevant properties for TE were identified in the printed samples. Firstly, stress-relaxation tests were performed to see if the incorporation of @rGOn had any mechanically reinforcing effect on the hydrogels. While variability between samples (height and diameter) of the same group was very high, the overall trend was an improved relaxation time for increased sample loading (0 wt.% 168 s; 2.5 wt.% 108 s; 5 wt.% 60 s). For future research it would be interesting to extract more comparable mechanical measurements such as a Young's or compressive modulus. Aside from more accurately establishing a good @rGOn content, it would also help determine a $CaCl_2$ concentration and immersion time for the post-print bath that results in hydrogels that better mimic the mechanical microenvironments of the native tissue.

Secondly, it was found that the @rGOn was only able to significantly increase the conductivity at the highest concentration (5 wt.%). Interestingly, the highest loading (5 wt.%) even reached conductivity levels in the range of pure graphene ($10^2 – 10^3$ S cm^{-1}). According to percolation theory of conducting composites, three states exist; insulating, when there is no contact between fillers (*i.e.,* low concentrations; conductivity of polymer), percolating, when there is no direct contact but electron tunneling may occur between fillers (*i.e.,* middle concentrations; increased conductivity), and conducting, with contact between fillers throughout (*i.e.,* higher concentrations; conductivity of filler) [59]. It is suspected that the highest concentration (5 wt.%) could reach the conducting state, while the other two (0, 2.5 wt.%) are still insulating. Overall, the conductivity of the samples was also high, but this might be attributed to some residual water left in the samples. Prior to testing, samples were dried in a vacuum oven (40 °C) over 3 days, yet some samples were still considerably damp. While these were not tested, the possibility that the visibly dry samples were not completely dehydrated cannot be excluded. To confirm, the experiment should be reperformed with completely dried samples and a pure film of @rGOn as control.

Lastly, the temperature increase under NIR radiation was lower in the scaffolds (2.5 wt.%, ΔT_{final} = 5.4 ± 0.04 °C; 5 wt.%, ΔT_{final} = 7.9 ± 1.4 °C) than for the dispersion (@rGOn, ΔT_{final} = 12.8 ± 0.2 °C). Despite that, this is not a bad result. Even at the lowest loading (2.5 wt.%) the samples approximately reach the minimum temperature (43 °C) for cancer hyperthermia therapy, which is controversial as greater effectiveness has been reported at lower temperatures [38]. Moreover, for TE, only slight increases in temperature (2-4 °C) have been shown to already positively affect osteogenesis through the upregulation of heat shock proteins [14, 15]. If a higher temperature increase would be desired, the first option would seem to reduce the porosity of the scaffold, thereby increasing the directly irradiated surface area. However, @rGOn-PEC (0, 2.5, 5 wt.%) discs showed no significant difference in ΔT with scaffolds (Supplementary Figure 2). Therefore, the porosity of the scaffold does not appear to have a great influence on its ability to convert NIR-light into heat. Nevertheless, it would be worthwhile to further investigate scaffolds of different porosities. For example, higher porosity will negatively affect the mechanical integrity of the sample but also improves the ability of nutrients to diffuse through samples. Additionally, lower pore sizes can promote cell adhesion and proliferation of human bone marrow stem cells (hMSCs) and could even help guide them into an osteogenic lineage [60, 61].

The @rGOn-PEC materials appear to not to cause cytotoxicity but more work is required to make definitive conclusions. While the indirect biocompatibility assay showed no decline in cell viability after exposure, in the final application cells will be directly attached to the @rGOn-PEC scaffolds. For now, there is not sufficient data exploring direct contact to make definitive statements about sample cytotoxicity. Before seeding cells, the samples were incubated overnight in FBS to absorb nutrients from the culture media to promote cell adhesion. However, it is likely that during this time monovalent ions from the media exchange with the Ca^{2+} ions in the hydrogel, which reduces its gelation strength and causes fragility in the scaffolds. This resulted in large differences between groups, premature breaking of the samples and overall conflicting data. For example, metabolic activity assay show a very large drop in cell viability for the 0 wt.% @rGOn group, whereas confocal images indicate the opposite with best cell attachment for that same group. Nevertheless, as a proof-of-concept, it demonstrates that cells are able to attach to the scaffolds, even when containing 2.5 wt.% @rGOn. Before repeating the experiment, however, further optimization will be required. Supplementation of Ca^{2+} ions to the culture media might be considered to reduce ion exchange. The initial polymer concentration in the hydrogel could be increased as well. The experiments could also be repeated with discs instead of scaffolds, to reduce variability between groups and for a longer period of time to allow the cells to completely cover the material.

Lastly, a substantial amount of work has been published on the biocompatibility and (bio-)degradation of GO and some on rGO. Yet, the biocompatibility of @rGOn particles is much less described. While, GO has been established as generally non-toxic material, rGO is only described as biocompatible in low concentrations. Moreover, the same degradation methods are unsuccessful for rGO [22]. Since we previously established that @rGOn is further reduced than GOn, it is not safe to say it is equally biocompatible and would probably be more related to rGO. However, compared to commonly reported sizes of rGO, these materials are smaller, which is beneficial for their biocompatibility and (bio-)degradation [62]. To provide more clarity, a biodegradation study is currently being performed. Additionally, in this work the nanosheets are encapsulated inside a hydrogel without direct contact to the cells, which also changes the situation. Therefore, all in all a lot more further studies into biocompatibility and (bio-)degradation are also required.

5 Conclusion

This work presents a composite material of magnetized graphene oxide nanoparticles (GOn) and pectin hydrogel. First, GOn were magnetized with iron nanoparticles, producing magnetic, reduced GOn (@rGOn) with an average particle size of 379.5 ± 161.2 nm, a saturation magnetization of 59.6 emu/g and maximum heating capacity under NIR irradiation of 12.8 ± 0.2 °C. Then, @rGOn particles were incorporated in a tuneable pectin (PEC) hydrogel, where the @rGOn content was shown not to affect the printability. However, crosslinking of PECMA or PECNOR samples after printing was not possible through photo-crosslinking methods, so a $CaCl_2$ bath was used to crosslink the hydrogels. Printing was optimized, producing scaffolds with an average fiber diameter of 1061 ± 25 μm, average pore size of 1306 ± 220 μm and a printing quality of 68.8 ± 3.6 %. Printed @rGOn-PEC scaffolds demonstrated a maximum saturation magnetization of 6.17 emu/g, considerably high conductivity (~$1.1 \cdot 10^5$ S/m) and retained moderate ability of NIR light-heat conversion (ΔT = 7.9 ± 1.4 °C), which is sufficient for mild hyperthermia purposes. Lastly, biocompatibility of the material was evaluated by indirect and direct methods, which give an indication that the material is not cytotoxic. However, much more research is necessary. Further work, would explore methods to more accurately determine the mechanical properties of the material, so the better crosslinking parameters can be determined. Moreover, further optimization is necessary before new cytotoxicity experiments can be done to ensure the samples remain sturdy when immersed in culture media. Then, it is essential that when next cytotoxicity test are performed, these are done for longer periods of time to allow the cells enough time to attach to the samples. Lastly, it would be interesting to see the cancer cell killing effects of NIR irradiation on the scaffolds, as well as the effects of an external magnetic field to provide a mechanical stimulus on attached cells. Overall, these results provide the first few steps towards a novel multi-responsive biomaterial for application in tissue engineering.

6 References

1. Lechler, R.I., et al., *Organ transplantation—how much of the promise has been realized?* Nature Medicine, 2005. **11**(6): p. 605-613.
2. Khademhosseini, A. and R. Langer, *A decade of progress in tissue engineering.* Nature Protocols, 2016. **11**(10): p. 1775-1781.
3. Kargozar, S., et al., *"Hard" ceramics for "Soft" tissue engineering: Paradox or opportunity?* Acta Biomaterialia, 2020. **115**: p. 1-28.
4. Boccaccini, A.R., P.X. Ma, and L. Liverani, *Tissue Engineering Using Ceramics and Polymers*. 2021: Elsevier Science.
5. Manoukian, O.S., et al., *Biomaterials for Tissue Engineering and Regenerative Medicine*, in *Encyclopedia of Biomedical Engineering*, R. Narayan, Editor. 2019, Elsevier: Oxford. p. 462-482.
6. Mertz, D., et al., *Nanocomposite Polymer Scaffolds Responding under External Stimuli for Drug Delivery and Tissue Engineering Applications.* Advanced Therapeutics, 2020. **3**(2): p. 1900143.
7. Saltzman, W.M. and W.L. Olbricht, *Building drug delivery into tissue engineering design.* Nature Reviews Drug Discovery, 2002. **1**(3): p. 177-186.
8. Kim, S.H., et al., *4D-bioprinted silk hydrogels for tissue engineering.* Biomaterials, 2020. **260**: p. 120281.
9. Hendrikson, W.J., et al., *Towards 4D printed scaffolds for tissue engineering: exploiting 3D shape memory polymers to deliver time-controlled stimulus on cultured cells.* Biofabrication, 2017. **9**(3): p. 031001.
10. Pramanik, N., et al., *Fabrication of magnetite nanoparticle doped reduced graphene oxide grafted polyhydroxyalkanoate nanocomposites for tissue engineering application.* RSC Advances, 2016. **6**(52): p. 46116-46133.
11. Panseri, S., et al., *Innovative magnetic scaffolds for orthopedic tissue engineering.* Journal of Biomedical Materials Research Part A, 2012. **100A**(9): p. 2278-2286.
12. Elkasabgy, N.A. and A.A. Mahmoud, *Fabrication Strategies of Scaffolds for Delivering Active Ingredients for Tissue Engineering.* AAPS PharmSciTech, 2019. **20**(7): p. 256.
13. Costa-Almeida, R., et al., *Near-Infrared Radiation-Based Mild Photohyperthermia Therapy of Non-Melanoma Skin Cancer with PEGylated Reduced Nanographene Oxide.* Polymers, 2020. **12**(8).
14. Tong, L., et al., *Near-infrared light control of bone regeneration with biodegradable photothermal osteoimplant.* Biomaterials, 2019. **193**: p. 1-11.
15. Wang, L., et al., *Mild hyperthermia-mediated osteogenesis and angiogenesis play a critical role in magnetothermal composite-induced bone regeneration.* Nano Today, 2022. **43**: p. 101401.
16. Dong, S., et al., *Magnetic Hyperthermia–Synergistic H2O2 Self-Sufficient Catalytic Suppression of Osteosarcoma with Enhanced Bone-Regeneration Bioactivity by 3D-Printing Composite Scaffolds.* Advanced Functional Materials, 2020. **30**(4): p. 1907071.
17. Liu, R., et al., *Polydopamine doped reduced graphene oxide/mesoporous silica nanosheets for chemo-photothermal and enhanced photothermal therapy.* Materials Science and Engineering: C, 2019. **96**: p. 138-145.
18. Guo, Z., et al., *Surface Functionalization of Graphene-Based Materials: Biological Behavior, Toxicology, and Safe-By-Design Aspects.* Advanced Biology, 2021. **5**(9): p. 2100637.

19. Lebepe, T.C., et al., *Graphene Oxide-Gold Nanorods Nanocomposite-Porphyrin Conjugate as Promising Tool for Cancer Phototherapy Performance.* Pharmaceuticals, 2021. **14**(12).
20. Fathi-Achachelouei, M., et al., *Use of Nanoparticles in Tissue Engineering and Regenerative Medicine.* Frontiers in Bioengineering and Biotechnology, 2019. **7**.
21. Azevedo, S., et al., *Advances in carbon nanomaterials for immunotherapy.* Applied Materials Today, 2022. **27**: p. 101397.
22. Kurapati, R., et al., *Degradation of Single-Layer and Few-Layer Graphene by Neutrophil Myeloperoxidase.* Angewandte Chemie International Edition, 2018. **57**(36): p. 11722-11727.
23. Mukherjee, S.P., et al., *Graphene oxide is degraded by neutrophils and the degradation products are non-genotoxic.* Nanoscale, 2018. **10**(3): p. 1180-1188.
24. Jasim, D.A., et al., *The Effects of Extensive Glomerular Filtration of Thin Graphene Oxide Sheets on Kidney Physiology.* ACS Nano, 2016. **10**(12): p. 10753-10767.
25. Bera, B., *A review on polymer, graphene and carbon nanotube: properties, synthesis and applications.* Imperial Journal of Interdisciplinary Research (IJIR), 2017. **3**(10): p. 61-70.
26. Lee, C., et al., *Measurement of the Elastic Properties and Intrinsic Strength of Monolayer Graphene.* Science, 2008. **321**(5887): p. 385-388.
27. Memarian, F., A. Fereidoon, and M. Darvish Ganji, *Graphene Young's modulus: Molecular mechanics and DFT treatments.* Superlattices and Microstructures, 2015. **85**: p. 348-356.
28. Sang, M., et al., *Electronic and Thermal Properties of Graphene and Recent Advances in Graphene Based Electronics Applications.* Nanomaterials, 2019. **9**(3): p. 374.
29. Fang, C., et al., *Calculating the Electrical Conductivity of Graphene Nanoplatelet Polymer Composites by a Monte Carlo Method.* Nanomaterials, 2020. **10**(6): p. 1129.
30. Timochenco, L., et al., *High-Yield Production of Nano-Lateral Size Graphene Oxide by High-Power Ultrasonication.* Materials, 2021. **14**(8).
31. Silva, F.A.L.S., et al., *Graphene Oxide Topical Administration: Skin Permeability Studies.* Materials, 2021. **14**(11).
32. MENDES, A.M.M. and D.A.P. Tanaka, *Composite grapheno-metal oxide platelet method of preparation and applications*. 2011, Google Patents.
33. Chua, C.K. and M. Pumera, *Chemical reduction of graphene oxide: a synthetic chemistry viewpoint.* Chem. Soc. Rev., 2014. **43**(1): p. 291-312.
34. Goenka, S., V. Sant, and S. Sant, *Graphene-based nanomaterials for drug delivery and tissue engineering.* Journal of Controlled Release, 2014. **173**: p. 75-88.
35. Shin, S.R., et al., *Graphene-based materials for tissue engineering.* Advanced Drug Delivery Reviews, 2016. **105**: p. 255-274.
36. Sundaram, P. and H. Abrahamse, *Phototherapy Combined with Carbon Nanomaterials (1D and 2D) and Their Applications in Cancer Therapy.* Materials, 2020. **13**(21).
37. Bai, G., et al., *Stimuli-Responsive Scaffold for Breast Cancer Treatment Combining Accurate Photothermal Therapy and Adipose Tissue Regeneration.* Advanced Functional Materials, 2019. **29**(36): p. 1904401.
38. Wust, P., et al., *Hyperthermia in combined treatment of cancer.* The Lancet Oncology, 2002. **3**(8): p. 487-497.
39. Ribeiro, C., et al., *Proving the suitability of magnetoelectric stimuli for tissue engineering applications.* Colloids and Surfaces B: Biointerfaces, 2016. **140**: p. 430-436.

40. Santos, L.J., R.L. Reis, and M.E. Gomes, *Harnessing magnetic-mechano actuation in regenerative medicine and tissue engineering.* Trends in Biotechnology, 2015. **33**(8): p. 471-479.
41. Gomes, M., et al., *Chapter 6 - Natural Polymers in tissue engineering applications*, in *Tissue Engineering*, C.v. Blitterswijk, et al., Editors. 2008, Academic Press: Burlington. p. 145-192.
42. Advincula, R.C., et al., *On the progress of 3D-printed hydrogels for tissue engineering.* MRS Communications, 2021. **11**(5): p. 539-553.
43. Munarin, F., et al., *Pectin-Based Injectable Biomaterials for Bone Tissue Engineering.* Biomacromolecules, 2011. **12**(3): p. 568-577.
44. Pereira, R.F., et al., *A single-component hydrogel bioink for bioprinting of bioengineered 3D constructs for dermal tissue engineering.* Materials Horizons, 2018. **5**(6): p. 1100-1111.
45. Munarin, F., M.C. Tanzi, and P. Petrini, *Advances in biomedical applications of pectin gels.* International Journal of Biological Macromolecules, 2012. **51**(4): p. 681-689.
46. Agarwal, T., M. Costantini, and T.K. Maiti, *Extrusion 3D printing with Pectin-based ink formulations: Recent trends in tissue engineering and food manufacturing.* Biomedical Engineering Advances, 2021. **2**: p. 100018.
47. Pereira, R.F., et al., *Cell-instructive pectin hydrogels crosslinked via thiol-norbornene photo-click chemistry for skin tissue engineering.* Acta Biomaterialia, 2018. **66**: p. 282-293.
48. Tortorella, S., et al., *Biocompatible pectin-based hybrid hydrogels for tissue engineering applications.* New Journal of Chemistry, 2021. **45**(47): p. 22386-22395.
49. Phan, L.M., et al., *Graphene Integrated Hydrogels Based Biomaterials in Photothermal Biomedicine.* Nanomaterials, 2021. **11**(4).
50. Shen, X., et al., *One-pot solvothermal syntheses and magnetic properties of graphene-based magnetic nanocomposites.* Journal of Alloys and Compounds, 2010. **506**(1): p. 136-140.
51. Chen, W., L. Yan, and P. Bangal, *Preparation of graphene by the rapid and mild thermal reduction of graphene oxide induced by microwaves.* Carbon, 2010. **48**: p. 1146-1152.
52. Neves, S.C., et al., *Biofunctionalized pectin hydrogels as 3D cellular microenvironments.* Journal of Materials Chemistry B, 2015. **3**(10): p. 2096-2108.
53. Rowley, J.A., G. Madlambayan, and D.J. Mooney, *Alginate hydrogels as synthetic extracellular matrix materials.* Biomaterials, 1999. **20**(1): p. 45-53.
54. Kurantowicz, N., et al., *Interaction of graphene family materials with Listeria monocytogenes and Salmonella enterica.* Nanoscale research letters, 2015. **10**: p. 23.
55. Sengupta, I., et al., *Thermal reduction of graphene oxide: How temperature influences purity.* Journal of Materials Research, 2018. **33**(23): p. 4113-4122.
56. Kumar, A. and C.K. Dixit, *3 - Methods for characterization of nanoparticles*, in *Advances in Nanomedicine for the Delivery of Therapeutic Nucleic Acids*, S. Nimesh, R. Chandra, and N. Gupta, Editors. 2017, Woodhead Publishing. p. 43-58.
57. Abid, et al., *Reduced graphene oxide (rGO) based wideband optical sensor and the role of Temperature, Defect States and Quantum Efficiency.* (2045-2322 (Electronic)).
58. Zhang, T., et al., *The UV absorption of graphene oxide is size-dependent: possible calibration pitfalls.* Microchimica Acta, 2019. **186**(3): p. 207.
59. Marsden, A.J., et al., *Electrical percolation in graphene–polymer composites.* 2D Materials, 2018. **5**(3): p. 032003.
60. Loh, Q.L. and C. Choong, *Three-dimensional scaffolds for tissue engineering applications: role of porosity and pore size.* Tissue engineering. Part B, Reviews, 2013. **19**(6): p. 485-502.

61. Brennan, C.M., K.F. Eichholz, and D.A. Hoey, *The effect of pore size within fibrous scaffolds fabricated using melt electrowriting on human bone marrow stem cell osteogenesis.* Biomedical Materials, 2019. **14**(6): p. 065016.
62. Bussy, C., H. Ali-Boucetta, and K. Kostarelos, *Safety Considerations for Graphene: Lessons Learnt from Carbon Nanotubes.* Accounts of Chemical Research, 2013. **46**(3): p. 692-701.

7 Supplementary Information

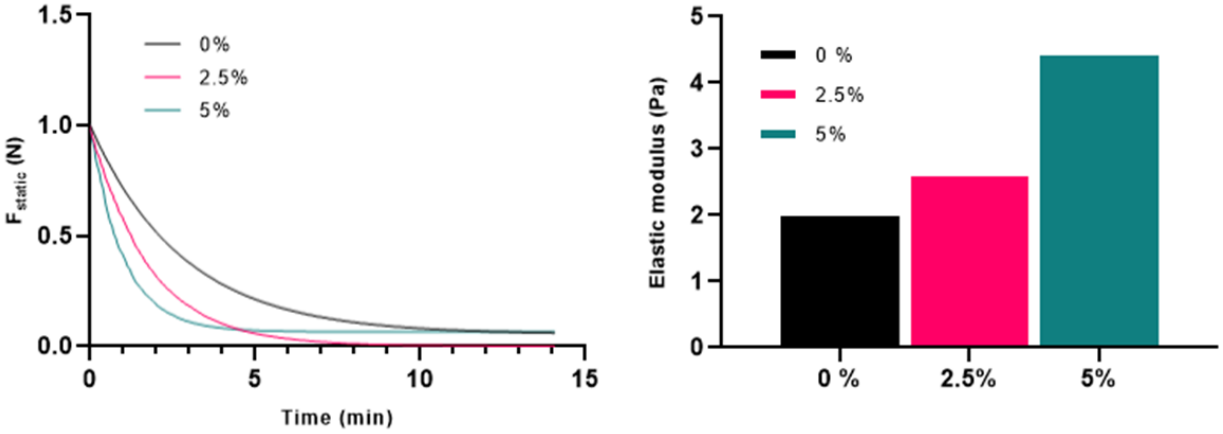

Figure S1: ***(left)*** **relaxation curves fit by exponential decay model and** ***(right)*** **initial rough estimates of elastic modulus based on the relaxation.**

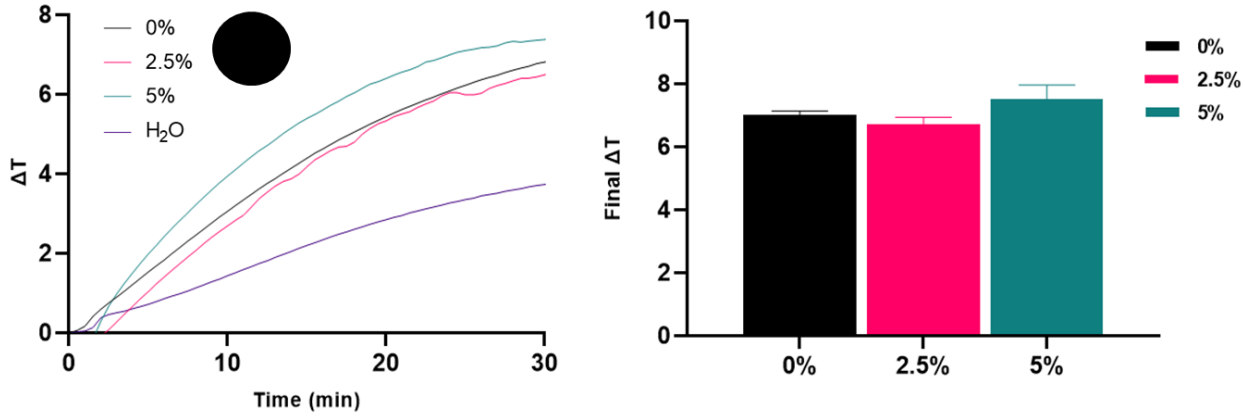

Figure S2: Change in temperature (ΔT) over time under near-infrared (NIR) irradiation and final ΔT after NIR irradiation for discs.

8 Related Work

Meneses, J., van de Kemp, T., Costa-Almeida, R., Pereira, R., Magalhães, F. D., Castilho, M., & Pinto, A. M. (2022). Fabrication of Polymer/Graphene Biocomposites for Tissue Engineering. Polymers, 14(5), 1038. MDPI AG. Retrieved from http://dx.doi.org/10.3390/polym14051038